Korean J. Chem. Eng., 38(8), 1648-1659 (2021)
DOI: 10.1007/s11814-021-0835-z

pISSN: 0256-1115
eISSN: 1975-7220

Enhanced performance of lanthanum orthoferrite/chitosan nanocomposites for adsorptive photocatalytic removal of Reactive Black 5

Muhd Arif Aizat Marhalim[*], Safia Syazana Mohtar[**], Abdussamad Mukhtar Mohammed[*,****], Farhana Aziz[*,**,†], Mohd Nazri Mohd Sokri[*,**], Wan Norharyati Wan Salleh[*,**], Norhaniza Yusof[*,**], Juhana Jaafar[*,**], Ahmad Fauzi Ismail[*,**], Madzlan Aziz[**,***], and Rosmawati Naim[*****]**

*School of Chemical and Energy Engineering, Faculty of Engineering, Universiti Teknologi Malaysia, 81310 Johor Bahru, Johor, Malaysia
**Advanced Membrane Technology Research Centre (AMTEC), Universiti Teknologi Malaysia, 81310 Johor Bahru, Johor, Malaysia
***Faculty of Science, Universiti Teknologi Malaysia, 81310 Johor Bahru, Johor, Malaysia
****Department of Chemistry, Yobe State University, Damaturu, Yobe State, Nigeria
*****Faculty of Chemical & Natural Resources Engineering, Universiti Malaysia Pahang, 26300 Kuantan, Pahang, Malaysia
(*Received 3 February 2021 • Revised 22 April 2021 • Accepted 3 May 2021*)

Abstract−New lanthanum orthoferrite ($LaFeO_3$)/chitosan nanocomposites were synthesized with different chitosan loadings (15 and 35%). Their adsorptive photocatalytic activity in the removal of Reactive Black 5 (RB5) was studied by manipulating the pH of the RB5 solution (pH 3, pH 6, pH 9), the catalyst loading (1 g L^{-1}, 2 g L^{-1}, and 3 g L^{-1}), and the initial concentration of RB5 (30 mg L^{-1}, 50 mg L^{-1}, and 70 mg L^{-1}) under 100 W LED light. The nanocomposites have a nanocrystalline structure similar to $LaFeO_3$ with a lower S_{BET} and P_V but a higher P_R. The $LaFeO_3$ was distributed well on chitosan matrices with variations in the elemental composition. The band gap was gradually decreased with increased chitosan loading. The nanocomposite with 15% chitosan loading (LC15) resulted as the most prominent photocatalyst with the highest removal of RB5 up to 98.5% under experimental conditions of pH 6, 2 g L^{-1} of catalyst loading, and 30 mg L^{-1} of initial RB5 concentration. The LC15 showed good stability, wherein the degradation efficiency was more than 90% after the fifth cycle with no significant change in the chemical properties. This work provides a technique to improve the removal of recalcitrant dyes through the processing of adsorptive photocatalysis utilizing adsorbent and perovskite.

Keywords: Adsorptive-photocatalysis, Chitosan, Lanthanum Orthoferrite, Reactive Black 5, Wastewater Treatment

INTRODUCTION

Textile processing is a particularly chemical-intensive process that involves the utilization of copious non-biodegradable, harmful chemicals. The unfixed chemicals by the fabrics (e.g., synthetic dyes, heavymetals, surfactants, and reducing agents) are discharged into waste stream. Azo dyes, the most commonly used colorants, account for 60 to 70% of all dyes [1]. They are synthetic compounds containing xenobiotic substitutions including sulfonic acid, azo, bromo, chloro, and nitro functional groups [2,3]. Even though these dyes have good fixation capability, it is reported that 10 to 15% could still be discharged [4]. The presence of these dyes in wastewater not only interferes with the photosynthetic function of plants severely but also affects the quality of freshwater. Furthermore, systematic absorption of these azo dyes has led to the production of hazardous aromatic amines via azoreductase activity of intestinal microflora by liver cells and skin surface bacteria [5].

Reactive Black 5 (RB5) dye is one of the most utilized azo dyes, contributing to more than 50% of total reactive dye demand [6,7]. This dye is highly soluble in water, able to form covalent bonds with fiber and contains chromophoric groups such as anthraquinone, azo, phthalocyanine, triarylmethane, oxazine, formazan, and so on [8]. The chemical structure, IUPAC name and general characteristics of this azo dye are summarized in Table 1. Since RB5 resists degradation, this aromatic and heterocyclic compound needs proper treatment to meet regulation requirements. Strategies on RB5 removal have been improvised year after year to find the ultimate solution for an efficient treatment. Such treatments include physical, chemical, thermal, and biological treatments. Adsorption, coagulation, filtration, reverse osmosis, evaporation, and chemical oxidation are among the commercially available methods that come with advantages and disadvantages [6,9-11].

Single ozonation process, a type of widely used chemical oxidation for dye wastewater treatment is facing some drawbacks, including incomplete oxidation and mineralization, low efficiency due to limited reaction kinetics and transport, high energy consumption that leads to high cost, and selectivity [12,13]. Thus, attention has been shifted to the heterogenous photocatalysis. Since its introduc-

†To whom correspondence should be addressed.
E-mail: farhanaaziz@utm.my

Table 1. Chemical structure, IUPAC name and general characteristics of RB5 [61]

Chemical structure	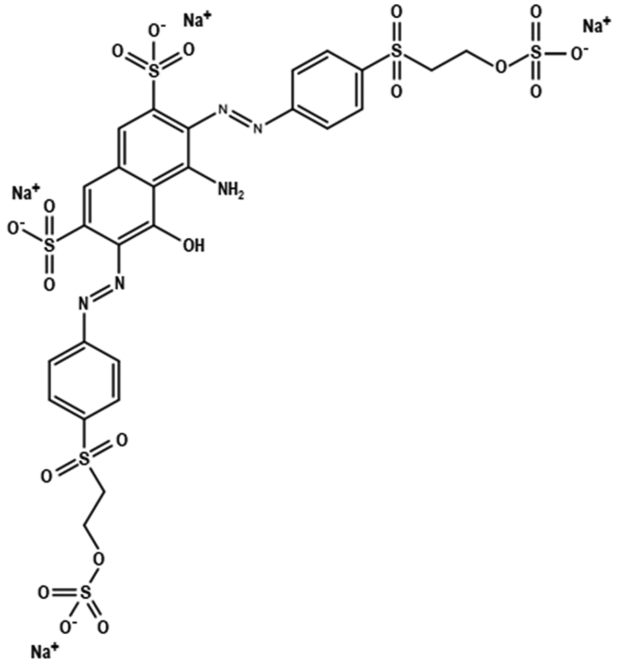
Chromophore	**-N=N-**
Molecular weight	991.82 g mol^{-1}
IUPAC name	Tetrasodium;4-amino-5-hydroxy-3,6bis[[4-(2-sulfonatooxyethylsulfonyl)phenyl]diazinyl]naphthalene-2,7-disulfonate
Molecular formula	$C_{26}H_{21}N_5Na_4O_{19}S_6$
Maximum absorption wavelength, λ_{max}	597 nm
Color index (C.I.) name	C.I. Reactive Black 5
Color index (C.I.) number	C.I. 20505
Application class	Cotton
Chemical class	Azo
CAS registry number	17095-24-8

tion in the 1970s, this treatment has been advancing greatly, becoming one of the most efficient treatment selections for recalcitrant wastewater. This process involves a change in the chemical reaction rate or its initiation under the action of light (i.e., ultraviolet, visible, or infrared) in the presence of a substance. To be specific, this process is associated with the electron (e^-) excitation of the valence band (VB) into the conduction band (CB) when the adsorbed photon energy is equal to or exceeds the band gap energy of applied photocatalytic materials. This process leaves a hole (h^+) in VB, inducing a charged recombination and transportation process, with the former process faster than the latter [14]. After the e^- and h^+ transfer to the active sites, they act as reducing or oxidizing agents to initiate reduction or oxidation on the surface. In depth, the oxidation of the organic compounds occurs by direct reaction with h^+ or indirect reaction with $OH^•$, which is formed by the reaction between h^+, adsorbed water, and hydroxyl ions, or free radicals [15].

One of the most promising and studied photocatalyst within AOPs treatment is titanium dioxide (TiO_2). TiO_2 is selected by many researchers because it is low-cost, chemically stable, non-toxic, environmentally friendly, and commercially available. However, due to its large band gap of ~3.2 eV, TiO_2 has limited light absorption in the UV region (~3.2 eV) [16]. Since UV light comprises only ~5% of the total solar irradiation with the remaining ~40% visible light and ~55% infrared, the use of TiO_2 results in a low efficiency in using sunlight. The transition of optical response from UV to visible region could have a significant positive effect on the applications [17]. Therefore, efforts on finding an alternative with small band gap have been carried out. Various photocatalytic materials such as ZnO, CuO, CeO_2, WO_3, Fe_2O_3, CdS, CuS, and Bi_2WO_6 have been reported to photodegrade organic dye contaminants [18-23]. Another potential photocatalyutic material that has been studied to overcome the drawbacks of TiO_2 is $LaFeO_3$. $LaFeO_3$ possesses a narrow band gap of 1.86 eV to 2.36 eV, making it more efficient under visible light compared to TiO_2. Furthermore, its stability and non-toxicity make it a promising material in wastewater treatment [24]. Several works related to the incorporation of TiO_2 and $LaFeO_3$ can be found in the literature. The hybrid design of heterojunction TiO_2/$LaFeO_3$ composites has great potential in enhancing its photocatalytic performance. A narrow bandgap $LaFeO_3$ is capable of extending the light absorption of the composite into the visible light region [25]. Furthermore, the incorporation enables the formation of p-n

junction on the interface, prolonging the lifetime of photogenerated carriers [26].

However, the susceptibility of $LaFeO_3$ to agglomeration hinders its single application in wastewater treatment research and study. This is mostly due to its high surface energy that interacts between the particles. Thus, scattering the nanoparticles onto a support material, which concurrently acts as an effective adsorbent, is an alternative way to reduce the agglomeration of the nanoparticles. Besides, the support material will also provide heterojunction for electron and holes that limits the charge recombination. To date, numerous support materials have been studied to support nanoparticles [27].

A perfect candidate to achieve this goal is the application of chitosan. Chitosan has excellent non-toxic, anti-microbial, biocompatible, and biodegradable properties, which are beneficial for many applications, such as tissue engineering, fuel cells, biodiesel, microbial encapsulation, cosmeceutical, agricultural, and food industry [28,29]. Chitosan also has been widely studied as adsorbent for water and wastewater treatment due to its high functional group contents (i.e., acetamido group, both primary hydroxyl and secondary hydroxyl group and amino group). These various functional groups provide a good base for interaction with other materials, such as metal oxides where multiple chemical bonds can be made to effectively improve the desired parameters and lower the band gaps or improve the distribution of nanoparticles in heterogenous photocatalysis studies [30-32].

In this study, for the first time, $LaFeO_3$ was integrated with chitosan via chemical precipitation method to produce high-performance nanocomposites for RB5 removal via synergistic adsorption-photocatalytic activities. The synthesized $LaFeO_3$, LC15, and LC35 were physicochemically characterized. The operational parameters for adsorptive-photocatalytic degradation, which were the initial pH of RB5 solution, nanocomposite loading, and initial concentration of RB5 solution were investigated. The dominant active species generated during the photocatalytic process were identified via scavenger experiment. The mechanism of RB5 photodegradation by the nanocomposite was also established. This study is important as it provides additional knowledge on the functions of chitosan adsorbents in enhancing the photocatalytic property of $LaFeO_3$ in degrading organic contaminants such as RB5.

EXPERIMENTAL

1. Materials

Ammonium oxalate (AO), chitosan (CAS 9012-76-4), iron(III) nitrate nonahydrate ($Fe(NO_3)_3{\cdot}9H_2O$, CAS 7782-61-8), lanthanum(III) nitrate hexahydrate ($La(NO_3)_3{\cdot}6H_2O$, CAS 10277-43-7), p-benzoquinone (p-BQ), and Reactive Black 5 (RB5, ≥50%, CAS 17095-54-8) were purchased from Sigma-Aldrich. Ammonia solution 25% was obtained from Merck. 2-propanol (2-PrOH), citric acid monohydrate ($C_6H_8O_7$), and sodium hydroxide (NaOH) were purchased from QRëc Chemicals. Glacial acetic acid (99%) was obtained from HmBG® Chemicals.

2. Synthesis of $LaFeO_3$ Nanoparticle

The synthesis of $LaFeO_3$ was by a gel-combustion method, following the previous study by [33,34] with some modifications. An equal molar of $La(NO_3)_3{\cdot}6H_2O$ and $Fe(NO_3)_3{\cdot}9H_2O$ was dissolved in a citric acid solution at 60 °C under stirring for 30 min. Then, an ammonia solution was added dropwise to neutralize and stabilize the solution. The nitrate-citrate solution was then poured into an aluminium tray and heated at 130 °C for 2 h to remove water and form a gel-like crystal. The solid was further heated at 200 °C overnight to be activated and transformed into loose powder (*i.e.*, $LaFeO_3$ nanoparticle). The $LaFeO_3$ nanoparticle was then collected and stored in a cool dark place to prevent unwanted photocorrosion.

3. Preparation of $LaFeO_3$-chitosan Nanocomposites

The synthesized $LaFeO_3$ and chitosan by the ratio of 85 : 15 (w/w) were added into 100 mL of 3% glacial acetic acid. The mixture was stirred at 60 °C for 30 min to allow a reaction between the chitosan and $LaFeO_3$. Then, 1 M of NaOH solution was added dropwise to precipitate the $LaFeO_3$-chitosan nanocomposite at pH 10. The supernatant was decanted after centrifugation at 3,500 rpm for 15 min and the precipitate was washed with deionized water and filtered. The washing process was repeated three times. Finally, the fabricated $LaFeO_3$-chitosan nanocomposite, denoted as LC15, was collected and dried in an oven at 60 °C for 24 h. The preparation process was repeated using $LaFeO_3$ to chitosan ratio of 65 : 35 (w/w) to obtain LC35 nanocomposite.

4. Photocatalytic Degradation Study

The adsorption-photocatalytic activity of LC15 and LC35 nanocomposites was studied using RB5 as a pollutant under visible light. The photocatalytic reactor was equipped with a blower fan, a magnetic stirrer, and a 100 W LED lamp as a visible light source. The photocatalytic study was conducted as follows. First, 1 g L^{-1} of the fabricated nanocomposite was added to 100 mL of 30 mg L^{-1} RB5 solution at pH 6. The dye solution in the presence of catalyst was kept in the dark for 2 h under stirring to achieve adsorption-desorption equilibrium. The mixture was then irradiated under visible light for 4 h. 3 mL of RB5 solution was collected every 60 min and filtered immediately using the 0.45 μm nylon-membrane syringe filter. The aliquot was analyzed by the Hach DR 5000 UV-vis laboratory spectrophotometer (Canada) to determine the final concentration. Normalized absorption of RB5 followed in λ=596 nm. The removal efficiency (%) of RB5 was calculated using Eq. (1),

$$\text{Removal efficiency} = \frac{C_0 - C_t}{C_0} \times 100 \quad (1)$$

where C_0 (mg L^{-1}) and C_t (mg L^{-1}) are the respective initial and final concentrations of RB5 at time t (h).

Three parameters were studied: initial pH of the RB5 solution (i.e., pH 3, pH 6 and pH 9), LC15 and LC35 loadings (i.e., 1 g L^{-1}, 2 g L^{-1}, and 3 g L^{-1}) and initial concentration of RB5 solution (i.e., 30 mg L^{-1}, 50 mg L^{-1}, and 70 mg L^{-1}).

5. Reusability and Scavenging Experiments

The reusability of nanocomposite was studied by running the photocatalytic experiment for five cycles under the experimental conditions of 1 g L^{-1} catalyst loading, pH 6, and 30 mg L^{-1} initial RB5 concentration. The initial and final concentrations of the RB5 solution were recorded for each cycle.

For the scavenging test, the photocatalytic experiment was carried out with the addition of 1 mmol of 2-PrOH, AO, and p-BQ separately under the experimental conditions of 1 g L^{-1} catalyst load-

ing, pH 6, and 30 mg L^{-1} initial RB5 concentration. The initial and final concentrations of RB5 were recorded. The experiment was repeated in the absence of scavenger, denoted as blank, as a comparative study.

6. Characterization Procedures

X-ray diffraction (XRD) patterns were analyzed using the x-ray diffractometer model PANalytical X'Pert PRO (Japan) with Cu Kα radiation. The average crystallite size of all samples was calculated from averaging the x-ray line broadening of the diffraction peaks using the following Scherrer equation:

$$D = \frac{0.89\lambda}{\beta\cos\theta} \quad (2)$$

where D (nm) is the crystallite size, λ (0.15406 nm) is the x-ray wavelength, β (rad) is full width at half-maximum (FWHM) of diffraction peak at 2θ, and θ (rad) is the Bragg's angle.

Fourier transform infrared spectroscopy (FTIR) spectra were recorded using the PerkinElmer FTIR (USA). The test was used to detect the presence and/or changes of functional groups in the nanocomposites. The specimen was examined in transmittance mode with a wavenumber range of 4,000 cm^{-1} to 400 cm^{-1} by employing the KBr technique.

Transmission electron microscopy (TEM) images were obtained by the JEOL model JEM-ARM200F atomic resolution analytical microscope (Japan). The analysis was carried out to determine the $LaFeO_3$ crystalline structure and behavior, lattice distance, and electron diffraction pattern.

Field emission scanning electron microscope (FESEM) images and energy-dispersive x-ray spectroscopy (EDX) analysis were carried out using Hitachi SU8020 (Japan) to study morphology and dispersal of $LaFeO_3$ and chitosan within the matrix, respectively.

Brunauer-Emmett-Teller (BET) analysis involved using AUTOSORB-IQ-MP (US) to identify the specific surface area (S_{BET}), pore volume (P_V), pore radius (P_R), and the adsorption isotherm of $LaFeO_3$, LC15, and LC35. The analysis was carried out at −195 °C of analysis bath temperature, 46.5 cm^3 of analysis free space, 0.13 psi of N_2 gas pressure, 0.12 psi of helium gas pressure, and 10 s of equilibration interval. The samples were initially prepared by heating at 150 °C in a vacuum space for 2 h.

The UV-vis diffuse reflectance spectroscopy (DRS) measurements were performed by the PerkinElmer Lambda 1050 UV-vis-NIR spectrophotometer (USA). The obtained results were converted to absorption spectra by using the Kubelka-Munk function and transformation as shown in Eq. (3),

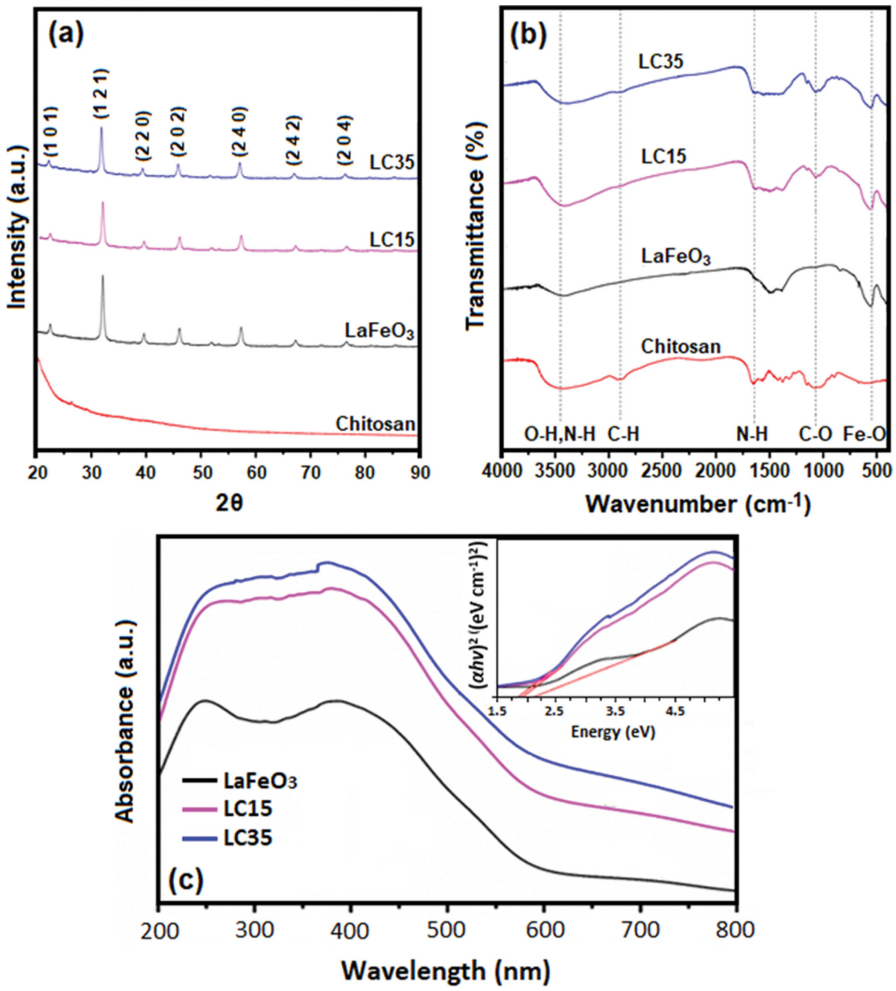

Fig. 1. (a) XRD patterns, (b) FTIR spectra of $LaFeO_3$, chitosan, LC15 and LC35, and (c) UV-vis spectra of $LaFeO_3$, LC15, and LC35.

$$F(R)=\frac{(1-R)^{n/2}}{2R}=\frac{K(\lambda)}{S(\lambda)}\propto a=\frac{(hv-E_g)^{n/2}}{hv} \quad (3)$$

where F(R) is the K-M function or re-emission function, R is the diffuse reflectance, K(λ) is the absorption coefficient, S(λ) is the scattering coefficient, hv (unit) is the photon energy, E_g (eV) is the band gap energy, n depends on the characteristics of optical transition (n=1 or 4 for direct or indirect band transition, respectively). It is commonly accepted that the n value for $LaFeO_3$ is 4. The hv was derived from hv=hc/λ, where h (eV) is Planck constant (4.136×10^{-15}), c (nm s^{-1}) is the light velocity in a vacuum (2.977×10^{17}), and λ (nm) is the wavelength.

RESULTS AND DISCUSSION

1. Characterizations of $LaFeO_3$, Chitosan, LC15, and LC35

1-1. Crystallinity Analysis

The XRD spectra of synthesized $LaFeO_3$ via the gel-combustion method in Fig. 1(a) show diffraction peaks at 2θ=22°, 32°, 39°, 46°, 57°, 67°, and 76°, which represent (101), (121), (220), (202), (240), (242) and (204) indexes, respectively. This can be indexed to the standard $LaFeO_3$ orthorhombic perovskite phase (Powder Diffraction File no. 37-1493). The strong and sharp diffraction peaks confirm the high crystallinity state of synthesized nanoparticles. As no possible impurities were detected, a successful synthesis of single-phase of $LaFeO_3$ at 200 °C via the gel-combustion method was achieved [34]. It is observed that the addition of chitosan did not change the crystallinity state of $LaFeO_3$ nanoparticles significantly since chitosan is a non-crystal biopolymer. A slight reduction in peaks intensity and broadening is observed for LC15 and LC35, which due to the reduction of nanocrystalline size [30]. The calculated crystalline size of $LaFeO_3$, LC15, and LC35 is presented in Table 2.

1-2. Functional Groups Analysis

As illustrated in Fig. 1(b), the FTIR spectrum of $LaFeO_3$ shows two distinctive peaks around 3,400 cm^{-1} and 550 cm^{-1}, representing O-H and Fe-O groups, respectively. The former represents the existence of water that might be absorbed from the surrounding humidity, while the stretching vibration around 550 cm^{-1} corresponds to the characteristic of the octahedral FeO_6 group in the perovskite compounds [27]. As $LaFeO_3$ nanoparticles made up the majority of the fabricated nanocomposites, changes in their structures determined the establishment of bonding and/or structural variations in the nanocomposites. Meanwhile, four distinctive peaks were observed for chitosan. The broad band around 3,400 cm^{-1} is due to the O-H and N-H stretching. The respective stretching bands at 2,900 cm^{-1} and 1,070 cm^{-1} are corresponding to the C-H symmetric and C-O stretching, which are the typical characteristics of polysaccharides. The band at 1,650 cm^{-1} represents the N-H bending of the primary amine [35].

The spectra of LC15 and LC35 are similar, with a distinct appearance of C-O, amino, and hydroxyl groups stretching vibrations of chitosan, indicating the strong attachment of chitosan particles to the $LaFeO_3$ nanoparticles [30]. The predominant change observed is the increasing intensity of the O-H group at 3,400 cm^{-1}, suggesting the formation of strong hydrogen bonding between the oxygen molecules in $LaFeO_3$ and the hydrogen molecules chitosan. The stretching intensity of the Fe-O group around 550 cm^{-1}, however, is slightly reduced particularly in the LC35 sample. This might be due to the strong interaction between $LaFeO_3$ and the chitosan matrix. The FTIR analyses confirm that the $LaFeO_3$-chitosan nanocomposites have been successfully synthesized.

1-3. Morphological and Elemental Analyses

As shown in Fig. 2(a), the TEM image of synthesized $LaFeO_3$ prepared by the gel-combustion method shows a random particle size with a crystalline structure. A high-resolution TEM (HRTEM) image as presented in Fig. 2(b) shows a uniform lattice fringe with an interplanar *d*-spacing of 0.272 nm assigned to (121) lattice planar, implying the formation of high quality orthorhombically-structured $LaFeO_3$ nanoparticles. On the other hand, the selected area electron diffraction (SAED) image as shown in Fig. 2(c), which was obtained from the interplanar *d*-spacing area, confirms the orthorhombic structure of $LaFeO_3$ and can be indexed to a standard powder diffraction data (JCPDS card no. 37-1493). These findings are consistent with the XRD analysis and findings by Li et al. [36]. The analysis by TEM for LC15 and LC35 nanocomposites was not carried out since their particle size was too large.

The FESEM images of $LaFeO_3$, chitosan, LC15, and LC35 are shown in Fig. 2(d) to (g). The image of $LaFeO_3$ displays porous nanostructures with irregular sizes and random dispersion. The irregular sizes and the fact that many nanoparticles were closely packed formed agglomeration caused by the auto-combustion method used for the synthesis of $LaFeO_3$ nanoparticles. Rapid decomposition of citric acid, which was used as a sacrificial agent, leads to strong redox reactions between $Fe(NO_3)_3{\cdot}9H_2O$ and $La(NO_3)_3{\cdot}6H_2O$, releasing gases such as nitrogen oxides (NO_x), carbon dioxide (CO_2) and water vapor (H_2O) [34,37]. As chitosan was added in the fabrication of LC15 in a lower ratio, it can be observed that $LaFeO_3$ nanoparticles dispersed on the surface of chitosan, reducing the agglomeration between nanoparticles, yet still in clumping manner. This observation justified the reduction of S_{BET} of the nanocomposites compared to $LaFeO_3$. When the ratio of chitosan increased in LC35, the clumping of $LaFeO_3$ sam-

Table 2. Crystallite size, BET surface area, pore radius, specific pore volume, and the elemental composition of LC15 and LC35 catalysts. Operating conditions: −195 °C of analysis bath temperature; 46.5 cm^3 of analysis free space; 0.13 psi of N_2 gas pressure; 0.12 psi of helium gas pressure; 10 s of equilibration interval

Element	Unit	$LaFeO_3$	LC15	LC35
La	(at%)	24.00	13.10	9.60
Fe	(at%)	23.50	11.90	10.80
O	(at%)	52.50	44.80	47.40
C	(at%)	-	27.30	27.40
N	(at%)	-	3.00	4.80
Textural characteristics				
Crystallite size	(nm)	16.00	15.16	15.87
S_{BET}	(m^2 g^{-1})	23.99	12.27	16.83
P_R	(nm)	4.23	2.05	1.95
$P_V\times10$	(cm^3 g^{-1})	1.30	1.17	1.02

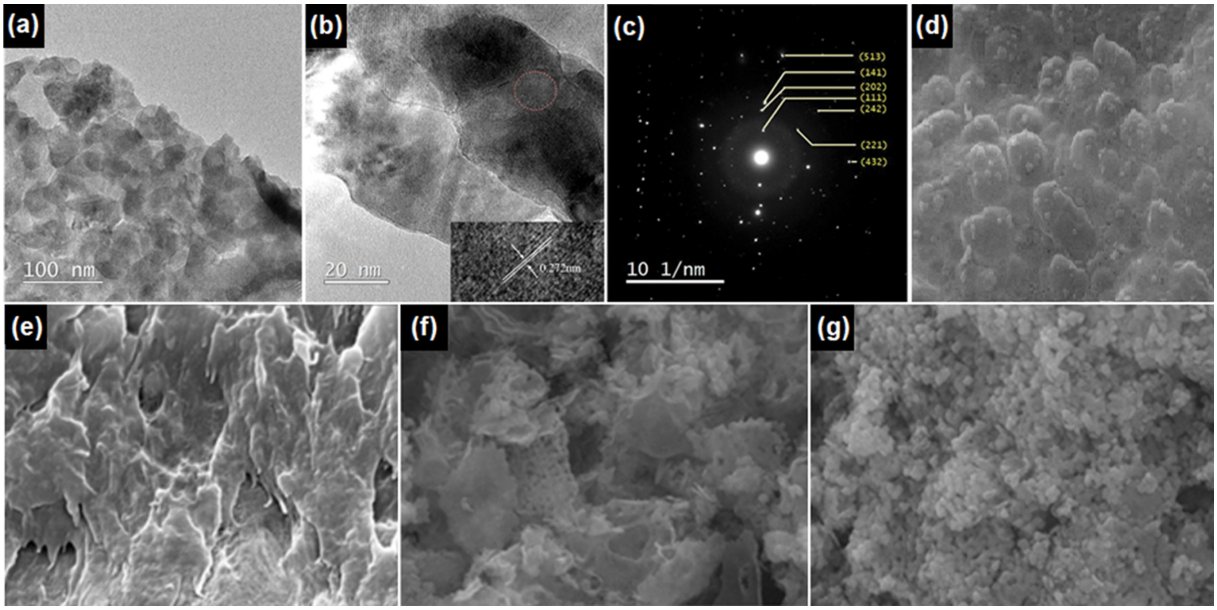

Fig. 2. Images of $LaFeO_3$ by (a) TEM, (b) HRTEM, (c) SAED, and (d) FESEM under x50000 magnification. FESEM images under x50000 magnification of (e) chitosan, (f) LC15, and (g) LC35 nanoparticles.

ples became more prominent. According to Saravanan et al., a higher amount of chitosan might lead to the dispersion of chitosan over the $LaFeO_3$, slightly decreasing the crystallinity of the nanoparticles, authorizing the results obtained from the XRD analysis [30]. Besides, the FESEM images supported the reduction in pore size obtained from the BET analysis data. A gradual increase of chitosan in the LC15 and LC35 nanocomposites tended to alleviate the agglomeration between $LaFeO_3$ nanoparticles, subsequently reducing the active surface area for photocatalytic activity.

The elemental composition of LC15 and LC35 analysis was carried out by the EDX. As shown in Table 2, the $LaFeO_3$ exhibits an atomic ratio of lanthanum (La) : iron (Fe) : oxygen (O) of about 1 : 1 : 3, which is the stoichiometric value for $LaFeO_3$. This ratio is important to highlight the purity of the nanoparticles as the presence of unwanted elements might compromise their photocatalytic activity [38]. The addition of chitosan in the fabrication of LC15 and LC35 nanocomposites reveals the presence of a high atomic percentage of carbon (C) atoms and an increased ratio of O compared to La and Fe atoms. This suggests the successful integration of chitosan and $LaFeO_3$ nanoparticles by strong hydrogen bonding between O atoms in $LaFeO_3$ and hydrogen (H) and nitrogen (N) atoms in chitosan, making up the hydroxyl (-OH) and amine ($-NH_2$) functional groups as observed in the FTIR spectra of LC15 and LC35 (Fig. 1(b)). The increased amount of chitosan increased the elemental C, N, and O but reduced the La and Fe elements.

1-4. Surface Area, Average Pore Radius, and Specific Pore Volume Analysis

The specific surface area and pore size of specific photocatalysts play a crucial role in determining their capability in adsorbing and degrading organic pollutants such as dyes. Based on Fig. S2, all samples show similar isotherms and hysteresis loops. According to the International Union of Pure and Applied Chemistry (IUPAC) classification, the resulting isotherms for all samples can be classified as Type IV isotherm with H3 hysteresis loop, a typical characteristic of mesoporous materials [39]. Mesoporous materials are materials containing pores with diameters between 2 nm to 50 nm, while materials with less than 2 nm pore diameter are considered as microporous materials. According to Sing and Yusof et al., the observed hysteresis loops are usually associated with capillary condensation in mesopore structures [40,41]. The H3 hysteresis loop sub-classification demonstrated their unlimited adsorption of nitrogen gas at high p/p^0 and the presence of slit-shaped pores due to aggregation of plate-like particles. Mesopores are favorable for photocatalytic applications over micropores because of their large surface area and the high number of pore sites, increasing the diffusion rate and eventually improving photocatalytic activity.

Based on Table 2, the addition of chitosan gradually reduced the S_{BET}, V_P, and P_R of the synthesized nanocomposites. According to Li et al., this phenomenon might arise from the modification effect on the mesoporous nature of $LaFeO_3$ nanoparticles as chitosan was incorporated [39]. The gradual reduction of P_R as the chitosan loading increased was caused by the agglomeration of nanoparticles and pore blockage. This reduced the active surface area that might affect the production of radicals contributing to an effective photocatalytic degradation of RB5.

1-5. Optical Property Analysis

Understanding the optical property of specific materials is of utmost importance for photocatalytic studies. This not only assists in determining the light absorption range and capability of the specific materials, but also determines the band gap for an effective generation of radicals, contributing to cascading the photocatalytic mechanism [42]. Referring to Fig. 1(c), $LaFeO_3$ shows good light absorption within a wide range of the light spectrum, particularly around 400 nm. The ability of $LaFeO_3$ to absorb a higher amount of light at certain wavelengths has also been observed by [43] and

[27], which could be ascribed to the electronic transition from the valence band (VB) to the conduction band (CB).

Meanwhile, LC15 and LC35 show higher intensities compared to $LaFeO_3$ for light absorption, which might be due to the background absorption of the biopolymer [30]. Based on the absorbance value, the band gap energy (E_g) of $LaFeO_3$, LC15, and LC35 is determined from the Tauc plot of $(\alpha h\nu)^2$ versus photon energy ($h\nu$) (inset illustration in Fig. 1(c)). The intercept of the tangent to the x-axis gives the estimated 2.1 eV, 1.91 eV, and 1.84 eV band gap energy for the respective $LaFeO_3$, LC15, and LC35. These results imply that there is a gradual reduction of band gap energy with the chitosan loading. The values also show that the $LaFeO_3$, LC15, and LC35 could be activated under visible light irradiation. These results are in agreement with Saravanan et al. [30]. According to their findings, the incorporation of chitosan into TiO_2 minimized the band gap of the studied photocatalysts, which allowed light to be absorbed in the visible light region. Furthermore, the band gap decreased with increased chitosan loading.

2. Photocatalytic Degradation of RB5

In this study, chitosan was integrated with $LaFeO_3$ for two main purposes: (i) improving the $LaFeO_3$ ability to absorb visible light; (ii) providing more adsorption sites to improve synergistic adsorption-photocatalytic removal of RB5. The parameters were fixed at pH 6, 1 g L^{-1} of catalyst loading, and 30 mg L^{-1} initial RB5 concentration. As shown in Fig. 4(a), RB5 is stable under visible light, indicated by the insignificant concentration reduction for the photolysis test (absence of catalysis). In the presence of catalysts, the adsorption process (in the dark) is enhanced with LC35, resulting in the highest RB5 removal, which is 8-fold increment compared to the bare $LaFeO_3$. Meanwhile, LC15 resulted in 68% removal after the adsorption process. The decrement in the RB5 concentration continued under the visible light irradiation resulting photodegradation of 98.5%, which is comparable to that of LC35.

As shown in Fig. 3(a), the chitosan itself has a high adsorption property. By incorporating this adsorbent with $LaFeO_3$, the adsorption capacity of $LaFeO_3$ increased significantly, exceeding the chitosan itself. The positively charged LC15 and LC35 surfaces are mainly introduced by the amine group in chitosan and could strongly adsorb the negatively charged RB5 molecules by electrostatic interaction [44,45]. The highest loading of chitosan in the LC35 resulted in the dominance of the adsorption process without the need for photocatalytic degradation assistance. Meanwhile, as irradiation of visible light takes place, the photodegradation of RB5 by LC15 is initiated, and subsequently increases the removal rate by catalyzing adsorbed dye compounds. Since the only LC15 exhibits photocatalytic activity, this catalyst is further used in the parameters study.

2-1. Effect of Initial pH of RB5 Solution

The varying pH values of solutions resulted in different photocatalytic reaction effects [46]. Thus, it is critical to determine the suitable pH range for an effective RB5 removal by LC15 and LC35 nanocomposites. In this study, the pH varied at 3, 6, and 9, while keeping the catalyst loading at 1 g L^{-1} and initial RB5 concentration at 30 mg L^{-1}. As shown in Fig. 4(a), high degradation is achieved at lower pH. The final photocatalytic degradation of RB5 at pH 3 and 6 is comparable, even though better degradation is

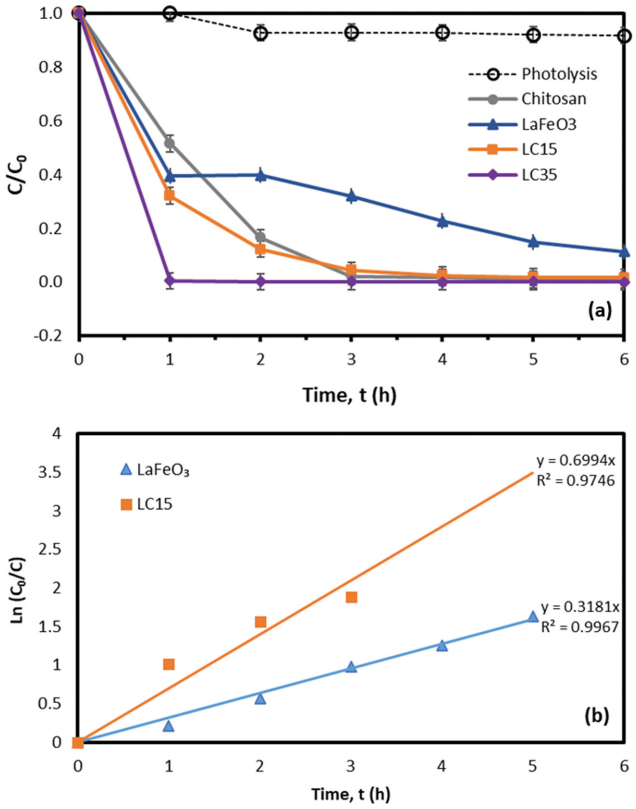

Fig. 3. (a) Adsorptive-photocatalytic degradation of RB5 by $LaFeO_3$, chitosan, LC15 and LC35 under the dark condition and visible light irradiation. Experimental conditions: 1 g L^{-1} catalyst loading; pH 6; 30 mg L^{-1} initial RB5 concentration and (b) linear plot of Ln(C_0/C) versus time for RB5 removal using $LaFeO_3$ and LC15.

shown during the adsorption process at pH 3. Contrarily, RB5 is unable to be degraded at a higher pH even in the presence of light.

It was reported that the zero point charge (pH_{zpc}) of chitosan is about 6.5 [47]. By increasing the pH of RB5 solution to basic condition, the LC15 nanocomposite surface, especially on the chitosan functional groups, is deprotonated. It is believed that there is a Coulombic repulsion between the negatively charged photocatalyst surface and the hydroxide (OH^-) anions, preventing the formation of •OH radicals. This subsequently reduces the photocatalytic degradation of dye [46]. In the meantime, although the adsorption rate of RB5 onto LC15 nanocomposites at pH 3 is higher than that of pH 6, the photocatalytic rate is lower. The high adsorption efficiency at a lower pH is a result of the higher electrostatic attraction of dye molecules onto the nanocomposite surfaces as the concentration of H^+ ions increased. However, as time progressed, the structural changes on LC15 nanocomposite caused by the dissociation of chitosan in acidic conditions, led to the agglomeration of nanoparticles. This lowered the availability of active sites for radicals' generations and thus reduced the photocatalytic rate. Therefore, pH 6 was chosen for further experiments.

2-2. Effect of Catalysts Loading

Optimum catalyst loading is important to prevent excessive usage of catalysts, leading to higher processing cost and to opti-

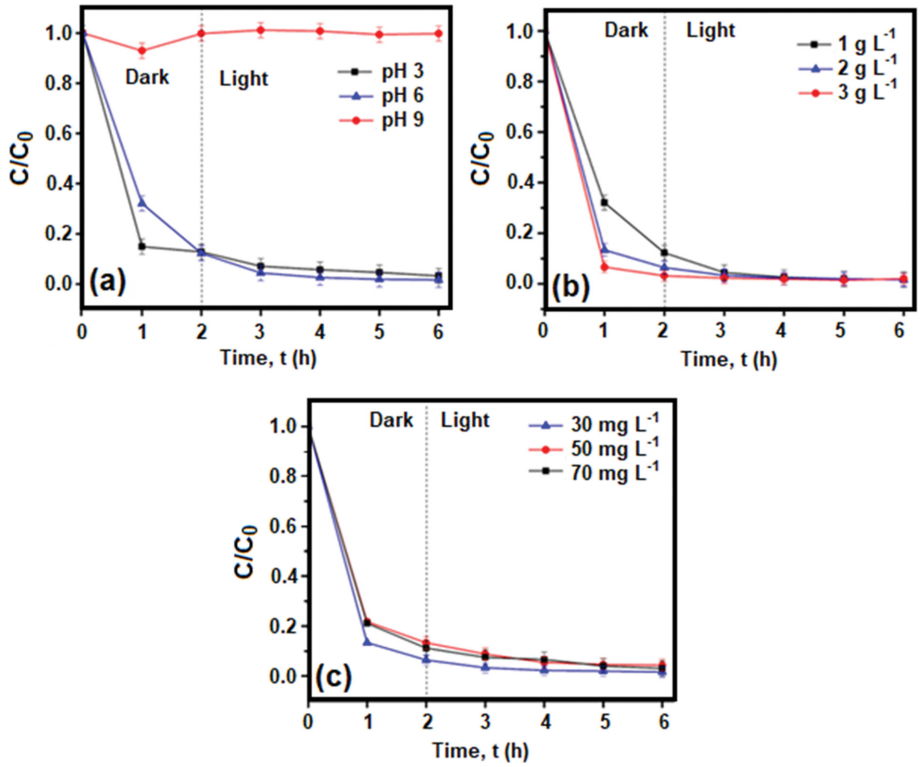

Fig. 4. Adsorptive-photocatalytic degradation of RB5 using LC15 nanocomposite by varying (a) initial pH of RB5 solution, fixed experimental parameters: 1 g L^{-1} catalyst loading; 30 mg L^{-1} initial RB5 concentration (b) catalyst loading, fixed experimental parameters: pH 6; 30 mg L^{-1} initial RB5 concentration, and (c) initial RB5 concentration, fixed experimental parameters: 2 g L^{-1} catalyst loading; pH 6.

mize the number of photons adsorbed onto the surface of the catalysts so the photocatalytic process can take place [48]. An excessive catalyst loading will subsequently reduce light penetration, resulting in the reduction of activated sites that negatively affect the overall performance of the photocatalytic process [49]. In this study, the catalyst loading was varied at 1 g L^{-1}, 2 g L^{-1}, and 3 g L^{-1}, while keeping the pH 6 and 30 mg L^{-1} initial RB5 concentration.

As shown in Fig. 4(b), almost all RB5 is removed after the photocatalytic reaction with different loadings. However, the adsorption rate increases with loading as the highest adsorption is 96% at 3 g L^{-1} of catalyst loading. The increasing amount of catalysts in the fixed concentration of RB5 provides more active sites for adsorption, causing a rapid decrement of RB5 concentration within the first hour without photocatalysis. However, further increment in catalyst loading may be insignificant or even detrimental to the photodegradation process due to the high possibility of nanoparticle agglomeration that reduces the number of vacant active sites for surface adsorption and photo-absorption [49].

2-3. Effect of the Initial Concentration of RB5

The effect of initial RB5 concentration was studied by manipulating the concentration at 30 mg L^{-1}, 50 mg L^{-1}, and 70 mg L^{-1}, while keeping the catalyst loading and initial pH constant at 2 g L^{-1} and pH 6, respectively. From Fig. 4(c), almost all RB5 is degraded at the end of the experiment for any initial RB5 concentration. 30 mg L^{-1} initial RB5 concentration, nonetheless, resulted in the highest removal rate as 98% of RB5 is degraded after 3 h.

In general, as the number of molecules increases with the initial dye concentration, the probability of catalyst-dye molecules interaction is reduced, which leads to the decrement in photocatalytic process efficiency [50]. However, in this study, variations in the initial concentration of RB5 resulted in a similar removal efficiency at the end of the experiment. Thus, the final RB5 degradation was determined through desorption process by changing the pH of the solution [51]. The pH of the RB5 solution was changed to pH 12 using 0.1 M NaOH to determine the actual decomposition of the RB5 compound. As illustrated in Fig. S3, 30 mg L^{-1} of initial RB5 concentration resulted in the lowest amount of desorption (i.e., ~1 mg L^{-1}), indicating the highest dye decomposition. While at 50 mg L^{-1} and 70 mg L^{-1} initial RB5 concentrations, high RB5 desorption up to 15 mg L^{-1} to 20 mg L^{-1} was obtained. This is because at a higher dye concentration, more dye molecules are adsorbed onto the catalyst surfaces, minimizing the availability of vacant active sites for radicals' generation. This resulted in more undecomposed dye molecules to be desorbed and traced in the aqueous solution [52].

3. Reusability Study

Other than studies regarding the photocatalytic efficiency under variation parameters, the reusability and stability of the fabricated nanocomposites are also important factors to be considered. It is due to the probability of photocorrosion or photodissolution to occur on the surface of the nanocomposite during photocatalysis, which gradually decreases the effectiveness [53]. The reusability of LC15 nanocomposite was examined by subjecting the nanocomposite to five consecutive cycles of RB5 removal under constant

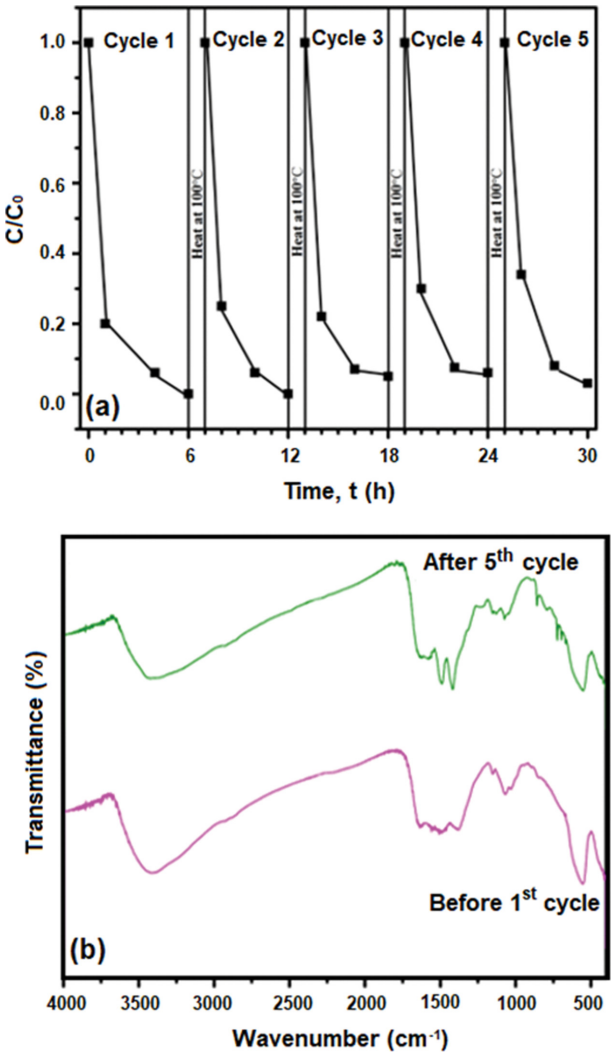

Fig. 5. (a) Five cyclic reusability test of LC15 nanocomposite at 1 g L^{-1} catalyst loading, pH 6, 30 mg L^{-1} initial RB5 concentration under visible-light irradiation and (b) FTIR spectra of LC15 nanocomposite before and after five cycles.

stirring at optimized conditions (i.e., pH 6, 30 mg L^{-1} of initial RB5 concentration and 2 g L^{-1} of LC15 loading). In this experiment, no washing step was carried out to eliminate the probability of (i) nanocomposites inevitable loss, (ii) catalyst reactivation, and (iii) vacancy of active sites that participate in the dye removal earlier. Moreover, the washing process is costly and time-consuming in real-life applications.

As presented in Fig. 5(a), there is only a slight reduction in the removal of RB5 by LC15 nanocomposite even after the fifth cycle. Furthermore, there are no changes of peaks when comparing the FTIR spectrum of LC15 nanocomposite before the experiment and after five consecutive cycles. These results confirm the superior reusability and stability of the fabricated nanocomposites. Meanwhile, according to Bilal et al., the RB5 characteristic peaks that could be detected by FTIR analysis include -CH_3 and -CH_2 asymmetric and symmetric vibrational stretching at 2,924 cm^{-1} and 2,854 cm^{-1}, C-C vibration of benzene at 1,609 cm^{-1}, N=N azo linkages at 1,458 cm^{-1}, and S=O vibrational stretch at 1,024 cm^{-1} [54]. Referring to Fig. 5(b), no introduction of the said peaks at these regions, proving the successful oxidation of RB5.

Since the washing step was skipped in this experiment, peaks of intermediate by-products are detected in the final spectrum. Strong stretching peaks in the regions between 1,490 cm^{-1} to 1,410 cm^{-1} are observed for nitro (N-O) (i.e., 1,490 cm^{-1}) and sulfate (S=O) (i.e., 1,415 cm^{-1} and 1,200 cm^{-1}) compounds [55]. These functional groups were introduced to the nanocomposite surface due to the formation of simple by-products with no trace of benzene rings nor the azo bonds (N=N), making the solution colorless and harmless. It is deduced that as the mixture was irradiated under visible light, the formed radicals started to degrade the dye molecules into smaller fragments, before further degrading them into CO_2 and water. However, as the cycle continued, the photocatalytic performance of the nanocomposites might have been reduced due to catalyst loss during the collection of aliquots, reducing the number of active photocatalysts (i.e., $LaFeO_3$) for the production of radicals, leaving some intermediate compounds or by-products not fully degraded and attached to the surface of LC15 nanocomposite.

As for the toxicity of the treated water, according to the cytotoxicity study by Bilal et al., there was a significant reduction in cell and shrimp mortality rate when incubated in treated RB5 solution with by-products detected [54]. They also stated that the high viability of the specimens was because most RB5 molecules were successfully transformed into CO_2, thus vanishing from the experiment. This proves that without the presence of azo bonds and benzene rings in the by-products formed, the toxicity level of the RB5 solution could be drastically reduced. Finally, as the main objective of this study was the total removal of RB5 by means of adsorption and photocatalysis, this result is not considered to be unacceptable per se, as the reusability tests were carried out without any washing steps or regeneration of the nanocomposites.

4. Kinetics and Mechanisms Studies

The kinetics of RB5 photodegradation by the $LaFeO_3$ and LC15 photocatalysts was studied based on the Langmuir-Hinshelwood model as shown in Eq. (3) [56]:

$$-\frac{dC}{dt} = k_r \frac{K_a C}{1 + K_a C} \tag{3}$$

where $-dC/dt$ is the degradation rate, C is the pollutant concentration, t is the reaction time, k_r is the rate constant, and K_a is the reactant adsorption coefficient. Since the initial concentration of RB5 was low (i.e., 30 mg L^{-1}), the K_a is negligible and Eq. (3) could be modified using the initial experimental conditions of $C=C_0$ at t=0 as [56]:

$$\mathrm{Ln}\left(\frac{C_0}{C}\right) = kt \tag{3}$$

where C_0 (mg L^{-1}) is the initial concentration of RB5 and k (h^{-1}) is the rate constant of the photocatalytic reaction, and t (h) is the time of photocatalytic reaction. The photodegradation kinetics of RB5 follows the pseudo-first order model depicted by the linear plot of $\mathrm{Ln}(C_0/C)$ versus time as depicted in Fig. 3(b). This result is consistent with the findings for most azo dye degradation in litera-

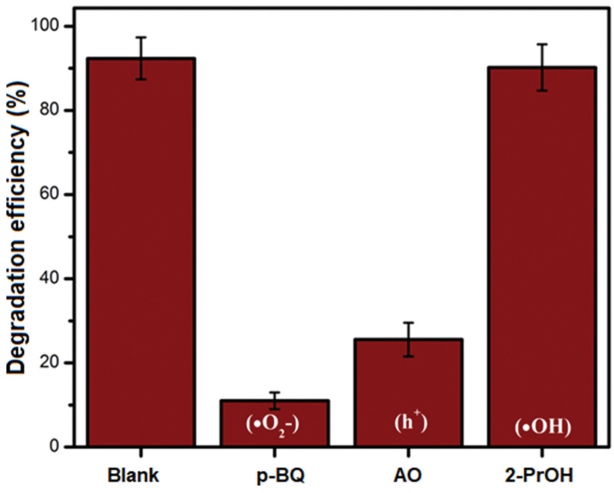

Fig. 6. Effect of various scavengers on the RB5 removal by LC15 nanocomposite under visible light irradiation. Experimental conditions: 1 g L^{-1} catalyst loading; pH 6; 30 mg L^{-1} initial RB5 concentration.

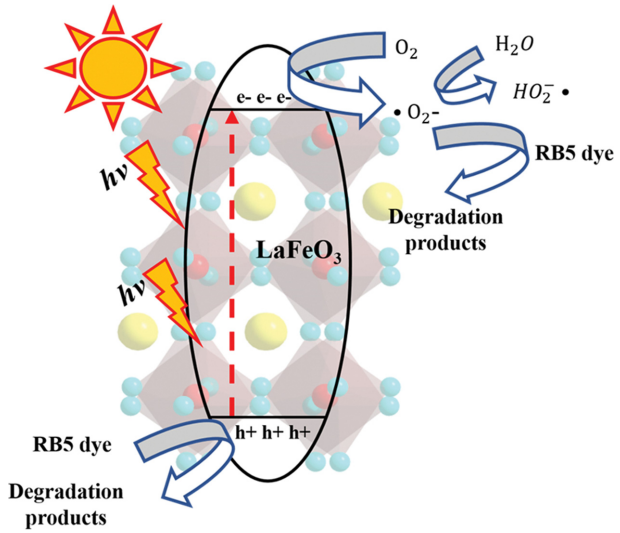

Fig. 7. Proposed mechanisms of visible light induced photocatalytic removal of RB5 by LC15 nanocomposite.

ture [57,58]. Accordingly, the reaction constants, k, for RB5 degradation using $LaFeO_3$ and LC15 were found to be 0.318 h^{-1} and 0.699 h^{-1}, respectively. LC35 was not considered in the kinetics study since it has reached equilibrium before the visible-light irradiation.

Scavenging experiments were conducted to investigate the principal active species in charge of the photodegradation of RB5. AO, 2-PrOH, and p-BQ were used as scavengers in the reaction system separately to determine the influence of hole (h^+), hydroxyl radical (•OH), and superoxide anion radical ($•O_2^-$) in the photocatalysis process [59]. As presented in Fig. 6, the high degradation of RB5 with the addition of 2-PrOH, suggested that the •OH radical is not a dominant active species. Meanwhile, the low removal of RB5 in the presence of p-BQ and OA implies that the h^+ and $•O_2^-$ are the main active species responsible for the photocatalytic degradation process.

Based on the experimental results, the plausible photocatalytic mechanism of RB5 removal through photocatalysis is proposed and the chemical reactions are as follows:

$$LC15+hv \rightarrow LC15\ (e^-_{CB}+h^+_{VB}) \quad (4)$$

$$h^+_{VB}+RB5\ molecules \rightarrow Degradation\ product \quad (5)$$

$$LC15\ (e^-_{CB})+O_2 \rightarrow •O_2^- \quad (6)$$

$$•O_2^-+RB5\ molecules \rightarrow Degradation\ product \quad (7)$$

$$•O_2^-+H_2O \rightarrow •HO_2^-+OH^- \quad (8)$$

$$HO_2^-+RB\%\ molecules \rightarrow Degradation\ product \quad (9)$$

$$•O_2^-+2H^++e^-_{CB} \rightarrow H_2O_2 \quad (10)$$

$$H_2O_2+RB5\ molecules \rightarrow Degradation\ product \quad (11)$$

In the photocatalysis process, the LC15 nanocomposite absorbs photon energy, which excites the electron from valence band (VB) to conduction band (CB), leaving the holes (h^+) at the VB (Eq. (4)). The transferred electrons react with adsorbed oxygen to form $•O_2^-$ radicals for pollutant degradation. Meanwhile, h^+ in the valence band (VB) could attack pollutants directly or react with H_2O/OH^- in the solution to form •OH radicals for pollutant degradation [60]. However, due to the less positivity of VB, adequate •OH species could hardly be generated for the individual dye degradation application. On the other hand, a high oxidative potential of photogenerated holes at the VB could result in direct oxidation and degradation of RB5 molecules (Eq. (5)).

Mohamed et al. indicated that hole oxidation could be simply initiated with sufficient adsorption of photocatalysts and a relatively high pollutant concentration on the catalyst surface, which might be applied to multiple photocatalysts with identical mechanism [59]. They also suggested that the increment in organic contaminant adsorption such as RB5 was caused by the strong π-π interactions and the relatively high photocatalyst surface area. Since the CB of $LaFeO_3$ in LC15 nanocomposite is hypothetically more negative, the photogenerated electrons can reduce the molecular oxygen into $•O_2^-$ (Eq. (6)). Furthermore, $•O_2^-$ may also react with water molecules (Eq. (8)) and H^+ (Eq. (10)) to form $•HO_2$ and H_2O_2, respectively, and degrade dye molecules (Eq. (11)). A schematic diagram of the overall separation and transition of photogenerated electron-hole pairs within LC15 matrices and photodegradation of RB5 molecules under visible light irradiation is illustrated in Fig. 7.

CONCLUSION

$LaFeO_3$-chitosan nanocomposites with different chitosan loading were successfully fabricated using a chemical precipitation method. Improvement in physicochemical properties was observed in LC15 and LC35 with some caveats, especially for the morphology of photocatalyst. LC15 shows a uniform distribution of $LaFeO_3$ on the chitosan matrix, while particle agglomeration is detected in LC35. Both nanocomposites show a reduction in the S_{BET} and P_R

as compared to $LaFeO_3$, but better RB5 removal efficiency, suggesting that the introduction of chitosan facilitates better dye molecules adsorption onto the surfaces of the nanocomposites. The LC15 shows an optimum photocatalytic activity at 30 mg L^{-1} of initial RB5 concentration at pH 6 and 2 g L^{-1} catalyst loading and is reusable. The photocatalytic pathway involves high reactive oxygen species than hydroxyl radicals, which is new to this field. These encouraging results imply the potential application of the fabricated photocatalysts in treating textile wastewater.

ACKNOWLEDGEMENTS

We gratefully acknowledge financial support from the Ministry of Higher Education, Malaysia under the Higher Institution Centres of Excellence (HiCOE) [Project No. R.J090301.7851.4J431] and Malaysian Research University Network (MRUN) [Project No. R.J130000.7813.4L874].

SUPPORTING INFORMATION

Additional information as noted in the text. This information is available via the Internet at http://www.springer.com/chemistry/journal/11814.

REFERENCES

1. G. Farshid and M. Mahsa, *Electrooxidation processes for dye degradation and colored wastewater treatment, Advanced nanomaterials for wastewater remediation*, CRC Press, Boca Raton, Florida (2016).
2. E. Petrucci, L. Di Palma, R. Lavecchia and A. Zuorro, *J. Ind. Eng. Chem.*, **26**, 116 (2015).
3. C. Ramírez, A. Saldaña, B. Hernández, R. Acero, R. Guerra, S. Garcia-Segura, E. Brillas and J. M. Peralta-Hernández, *J. Ind. Eng. Chem.*, **19**, 571 (2013).
4. F. M. D. Chequer, D. Dorta and D. P. D. Oliveira, in *Advances in treating textile effluent*, P. Hauser Ed., IntechOpen, London, United Kingdom (2011).
5. S. Nikfar and M. Jaberidoost, in *Encyclopedia of toxicology* (Third Edition), P. Wexler Ed., Academic Press, Oxford (2014).
6. L. Semiz, *Polym. Bull.*, **77**, 3047 (2020).
7. A. Garg, V. K. Sangal and P. K. Bajpai, *Desalin. Water Treat.*, **57**, 18003 (2016).
8. M. El Bouraie and W. S. El Din, *Sustain. Environ. Res.*, **26**, 209 (2016).
9. S. Çınar, Ü. H. Kaynar, T. Aydemir, S. Ç. Kaynar and M. Ayvacıklı, *Int. J. Biol. Macromol.*, **96**, 459 (2017).
10. B. Erdem, M. Erdem and A. S. Özcan, *Adsorption*, **22**, 767 (2016).
11. L. Wojnárovits and E. Takács, *Radiat. Phys. Chem.*, **77**, 225 (2008).
12. P. Pocostales, P. Álvarez and F. J. Beltrán, *Chem. Eng. J.*, **168**, 1289 (2011).
13. Y.-F. Rao, H.-J. Luo, C.-H. Wei and L.-F. Luo, *J. Cent. South Univ. Technol.*, **17**, 300 (2010).
14. Y. Wang, Q. Wang, X. Zhan, F. Wang, M. Safdar and J. He, *Nanoscale*, **5**, 8326 (2013).
15. A. G. Gutierrez-Mata, S. Velazquez-Martínez, A. Álvarez-Gallegos, M. Ahmadi, J. A. Hernández-Pérez, F. Ghanbari and S. Silva-Martínez, *Int. J. Photoenergy*, **2017**, 27 (2017).
16. M. N. Chong, B. Jin, C. W. K. Chow and C. Saint, *Water Res.*, **44**, 2997 (2010).
17. P. Foukal, *Solar astrophysics*, John Wiley & Sons, New York (1990).
18. A. A. M. Sakib, S. M. Masum, J. Hoinkis, R. Islam and M. A. I. Molla, *J. Compos. Sci.*, **3**, 91 (2019).
19. A. Mohagheghian, S.-A. Karimi, J.-K. Yang and M. Shirzad-Siboni, *J. Adv. Oxid. Technol.*, **18**, 61 (2015).
20. A. Fouda, S. E.-D. Hassan, E. Saied and M. S. Azab, *J. Environ. Chem. Eng.*, **9**, 104693 (2021).
21. E. M. Hashem, M. A. Hamza, A. N. El-Shazly, S. A. Abd El-Rahman, E. M. El-Tanany, R. T. Mohamed and N. K. Allam, *Chemosphere*, **277**, 128730 (2021).
22. M. M. Sabzehmeidani, H. Karimi and M. Ghaedi, *Polyhedron*, **170**, 160 (2019).
23. K. Villa, L. Děkanovský, J. Plutnar, J. Kosina and M. Pumera, *Adv. Funct. Mater.*, **30**, 2007073 (2020).
24. S. Thirumalairajan, K. Girija, N. Y. Hebalkar, D. Mangalaraj, C. Viswanathan and N. Ponpandian, *RSC Adv.*, **3**, 7549 (2013).
25. M. Humayun, Y. Qu, F. Raziq, R. Yan, Z. Li, X. Zhang and L. Jing, *Environ. Sci. Technol.*, **50**, 13600 (2016).
26. S. Xiang, Z. Zhang, C. Gong, Z. Wu, L. Sun, C. Ye and C. Lin, *Mater. Lett.*, **216**, 1 (2018).
27. K. Peng, L. Fu, H. Yang and J. Ouyang, *Sci. Rep.*, **6**, 19723 (2016).
28. S. K. Shukla, A. K. Mishra, O. A. Arotiba and B. B. Mamba, *Int. J. Biol. Macromol.*, **59**, 46 (2013).
29. P. Pal, A. Pal, K. Nakashima and B. K. Yadav, *Chemosphere*, **266**, 128934 (2021).
30. R. Saravanan, J. Aviles, F. Gracia, E. Mosquera and V. K. Gupta, *Int. J. Biol. Macromol.*, **109**, 1239 (2018).
31. L. Al-Naamani, S. Dobretsov, J. Dutta and J. G. Burgess, *Chemosphere*, **168**, 408 (2017).
32. M. A. Ahmed, N. M. Abdelbar and A. A. Mohamed, *Int. J. Biol. Macromol.*, **107**, 1046 (2018).
33. X. Qi, J. Zhou, Z. Yue, Z. Gui and L. Li, *Mater. Chem. Phys.*, **78**, 25 (2003).
34. X. Hao and Y. Zhang, *Mater. Lett.*, **197**, 120 (2017).
35. M. Queiroz, K. Melo, D. Sabry, G. Sassaki and H. Rocha, *Mar. Drugs*, **13**, 141 (2014).
36. L. Li, X. Wang and Y. Zhang, *Mater. Res. Bull.*, **50**, 18 (2014).
37. K. M. Parida, K. H. Reddy, S. Martha, D. P. Das and N. Biswal, *Energy*, **35**, 12161 (2010).
38. A. Aizat, F. Aziz, M. Z. M. Yusop, J. Jaafar, N. Yusof, W. N. W. Salleh and A. F. Ismail, *Mal. J. Fund. Appl. Sci.*, **15**, 462 (2019).
39. C. Li, S. Yu, H. Dong, C. Liu, H. Wu, H. Che and G. Chen, *Appl. Catal. B*, **238**, 284 (2018).
40. K. Sing, *Pure Appl. Chem.*, **54**, 2201 (1982).
41. N. F. Yusof, F. S. Mehamod and F. B. M. Suah, *J. Environ. Chem. Eng.*, **7**, 103007 (2019).
42. B. Ohtani, *Phys. Chem. Chem. Phys.*, **16**, 1788 (2014).
43. S. Acharya, D. K. Padhi and K. M. Parida, *Catal. Today*, **353**, 220 (2020).
44. Y. Zhu, S. Xu and D. Yi, *React. Funct. Polym.*, **70**, 282 (2010).
45. Y. Li, A. Lu, C. Wang and X.-L. Wu, *Sol. Energy Mater. Sol. Cells*, **92**, 953 (2008).
46. U. G. Akpan and B. H. Hameed, *J. Hazard. Mater.*, **170**, 520 (2009).

47. M. A. Torres, M. M. Beppu and C. C. Santana, *Braz. J. Chem. Eng.*, **24**, 325 (2007).
48. P. Kanhere and Z. Chen, *Molecules*, **19**, 19995 (2014).
49. A. Shet and K. V. Shetty, *Environ. Sci. Pollut.*, **23**, 20055 (2016).
50. R. G. Saratale, H. S. Noh, J. Y. Song and D. S. Kim, *J. Environ. Sci. Heal. A*, **49**, 1542 (2014).
51. M. Janus, E. Kusiak-Nejman and A. W. Morawski, *React. Kinet. Mech. Cat.*, **103**, 279 (2011).
52. A. A. Dougna, B. Gombert, T. Kodom, G. Djaneye-Boundjou, S. O. B. Boukari, N. K. V. Leitner and L. M. Bawa, *J. Photoch. Photobio. A*, **305**, 67 (2015).
53. Y. Wu, H. Wang, W. Tu, Y. Liu, Y. Z. Tan, X. Yuan and J. W. Chew, *J. Hazard. Mater.*, **347**, 412 (2018).
54. M. Bilal, T. Rasheed, H. M. N. Iqbal, H. Hu, W. Wang and X. Zhang, *Environ. Manage.*, **61**, 171 (2018).
55. E. Ivanchina, E. Ivashkina, I. Dolganova, E. Frantsina and I. Dolganov, *Chem. Eng. J.*, **329**, 250 (2017).
56. G. M. Neelgund, V. N. Bliznyuk and A. Oki, *Appl. Catal. B*, **187**, 357 (2016).
57. N. Yahya, F. Aziz, J. Jaafar, W. J. Lau, N. Yusof, W. N. W. Salleh, A. F. Ismail and M. Aziz, *Arab. J. Sci. Eng.*, **46**, 6153 (2021).
58. M. H. Habibi, A. Hassanzadeh and S. Mahdavi, *J. Photoch. Photobio. A*, **172**, 89 (2005).
59. M. A. Mohamed, M. F. M. Zain, L. J. Minggu, M. B. Kassim, N. A. S. Amin, W. N. W. Salleh, M. N. I. Salehmin, M. F. Md Nasir and Z. A. M. Hir, *Appl. Catal. B*, **236**, 265 (2018).
60. X. Liu and L. Cai, *Appl. Surf. Sci.*, **483**, 875 (2019).
61. M. R. J. Sarvestani and Z. Doroudi, *J. Water Environ. Nanotechnol.*, **5**, 180 (2020).

Supporting Information

Enhanced performance of lanthanum orthoferrite/chitosan nanocomposites for adsorptive photocatalytic removal of Reactive Black 5

Muhd Arif Aizat Marhalim[*], Safia Syazana Mohtar[**], Abdussamad Mukhtar Mohammed[*,****], Farhana Aziz[*,**,†], Mohd Nazri Mohd Sokri[*,**], Wan Norharyati Wan Salleh[*,**], Norhaniza Yusof[*,**], Juhana Jaafar[*,**], Ahmad Fauzi Ismail[*,**], Madzlan Aziz[**,***], and Rosmawati Naim[*****]**

*School of Chemical and Energy Engineering, Faculty of Engineering, Universiti Teknologi Malaysia, 81310 Johor Bahru, Johor, Malaysia
**Advanced Membrane Technology Research Centre (AMTEC), Universiti Teknologi Malaysia, 81310 Johor Bahru, Johor, Malaysia
***Faculty of Science, Universiti Teknologi Malaysia, 81310 Johor Bahru, Johor, Malaysia
****Department of Chemistry, Yobe State University, Damaturu, Yobe State, Nigeria
*****Faculty of Chemical & Natural Resources Engineering, Universiti Malaysia Pahang, 26300 Kuantan, Pahang, Malaysia
(*Received 3 February 2021 • Revised 22 April 2021 • Accepted 3 May 2021*)

Experimental Design

As depicted in Fig. S1, the experimental works were divided into three main parts: (1) synthesis of $LaFeO_3$ nanoparticles; (2) fabrication of $LaFeO_3$-chitosan nanocomposites; (3) performance tests. The synthesis $LaFeO_3$ and fabricated $LaFeO_3$-chitosan nanocomposites were characterized. The performance of the $LaFeO_3$-chitosan nanocomposites for RB5 removal was investigated by manipulating the pH of the RB5 solution, catalyst loading, and initial concentration of RB5 solution. The experimental conditions with the highest photodegradation performance were used to study the photocatalyst's stability and mechanisms.

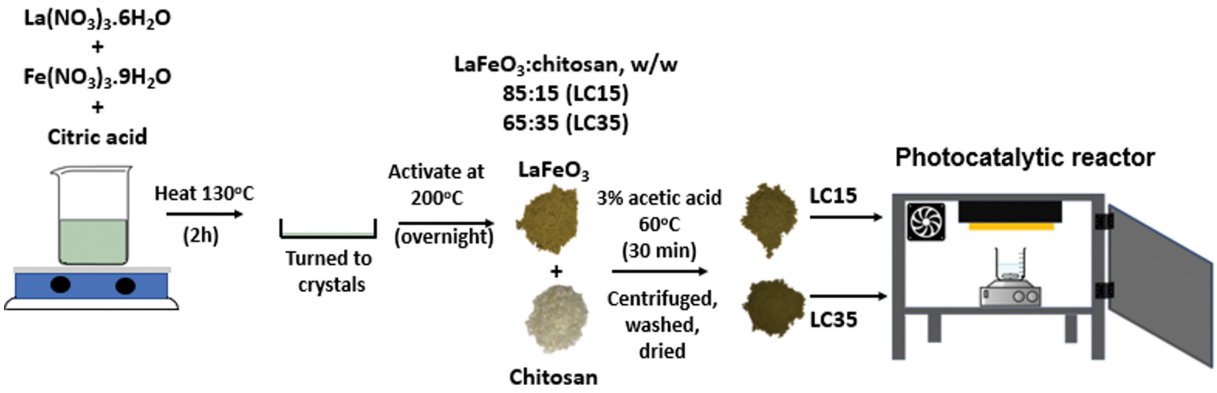

Fig. S1. Schematic diagram of experimental procedures.

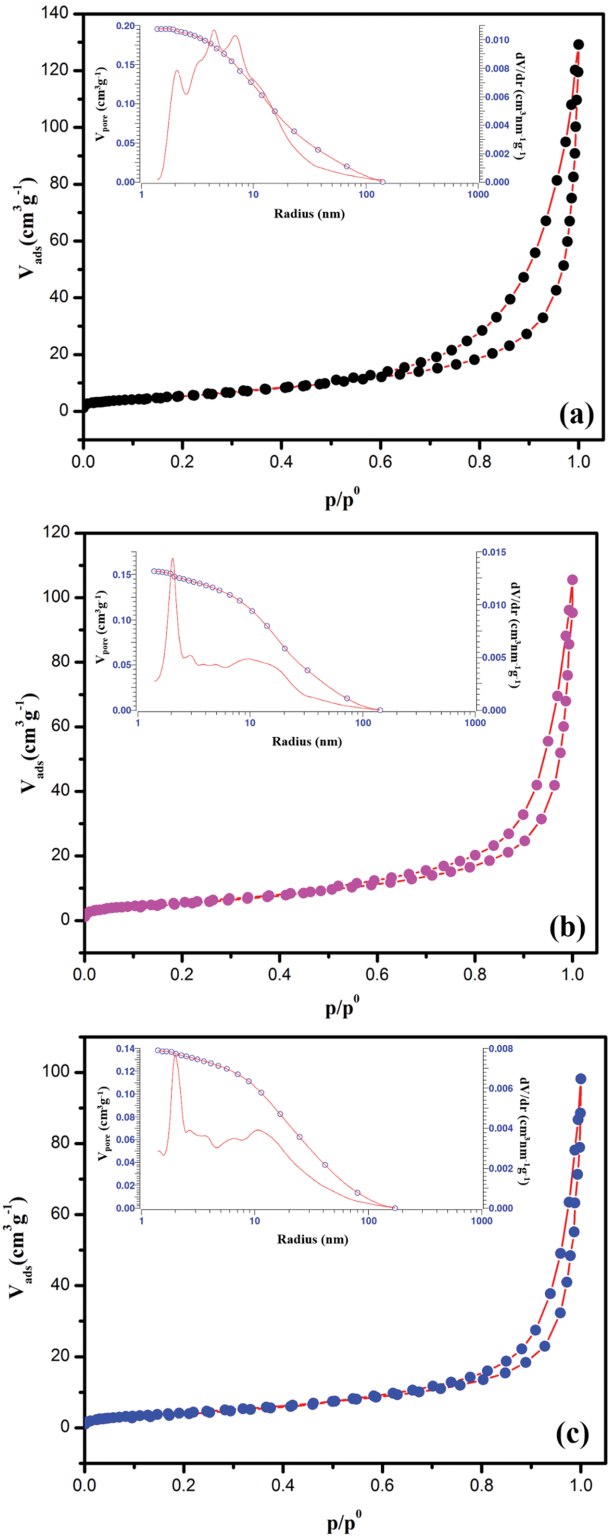

Fig. S2. Nitrogen adsorption-desorption isotherms and BJH pore radius distribution curve for (a) $LaFeO_3$, (b) LC15, and (c) LC35 nanocomposites.

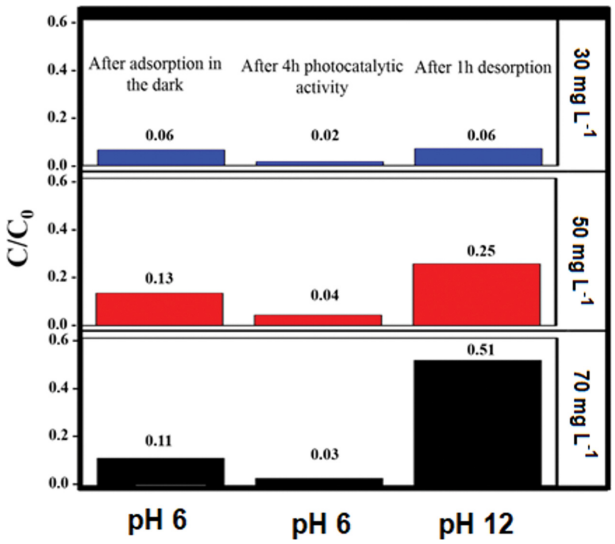

Fig. S3. Adsorption desorption illustration of results for different initial concentration of RB5 dye.